

Hygroscopy of Single-Stranded DNA Nano-Brushes: Atomic Workings of its Hydration-Induced Deformation

Maria Ortega, J. G. Vilhena,* and Rubén Pérez*

Hydration control of structure and mechanical properties is a process widely exploited in living organisms for key biological functions and, most recently, also in man-made smart materials. Here, the challenge of unveiling the underlying atomistic mechanisms of this phenomenon using all-atom Molecular Dynamics (MD) simulations to model the hygroscopic properties of polymer-brushes composed by single-stranded DNA (ssDNA) molecules is faced. The simulations identify three swelling regimes with a markedly different mechanical response. This evolution is produced by the competition between the formation of additional water–ssDNA and water–water hydrogen bonds, in a subtle interplay with the co-evolving structure of the ssDNA SAM. This cooperative interaction between conformational and hydration degrees of freedom should be applicable to other polymer brushes and related hydrogen-bonded systems. The results have direct implications for the use of ssDNA SAMs as sequencing devices, explaining the crucial role of the polymer-brush density in the SAM collective response to hydration, and for the alternative design of hygroscopic materials, that exploit the extreme hygroscopic power of biological polymers like ssDNA brushes.

1. Introduction

Water ubiquitous presence at ambient conditions makes its study a matter of utmost practical interest.^[1] In particular, a better understanding of both its structural^[2–6] and dynamic^[6–13] properties at interfaces has fueled advances in a manifold of areas, including: sensing,^[14] catalysis,^[15] tribology,^[16] protein adhesion,^[17] and among others.^[6] Likewise, the burgeoning field of smart-materials^[14,18–23] would also benefit from a more detailed (atomic) understanding of hydration properties.^[1,18]

This is especially apparent in hydration-induced self-morphing materials (also known as shape-memory materials).^[24–27] Although mechanisms are varied, most designs consist^[18] in harnessing hygroscopic properties of materials to program anisotropic (shape-shifting) hydration-induced swelling.

Hinging on such designing principle, spectacular examples can be found in the literature,^[14,24–27] ranging from macro-scale artificial muscles—exerting extraordinary forces only through hydration changes^[28,29], up to nanoscale polymer-brushes composed by single-stranded DNA (ssDNA), that have enabled the detection of single nucleotide mutations on a DNA sequence.^[14,30–34] However, a lack of atomistic insight into how water molecules regulate such reversible deformations has hampered a practical application of many of such devices.^[31,35,36]

Particularly, in the latter of the aforementioned examples,^[14] the capability to detect single nucleotide mutations severely depended on ssDNA length (limiting its DNA sequencing ability) and the polymer-brush density (limiting the device-response reproducibility and thus its practical use).^[31,35,36]

Molecular dynamics (MD) is one of the most widely used methods to unveil dynamic and non-equilibrium atomic processes at the nanoscale.^[12,13,37–39] MD simulations may provide a unmatched multi-scale picture, ideally bridging pico-second dynamics of single water molecules with single-fiber deformations extended over several nanometers that lead to micro-scale changes in shape and size.^[18,40] Hydration effects have been studied with atomistic detail in the case of polyethylene glycol (PEG), a structurally simple and water-soluble polymer that is widely used in medical and pharmaceutical applications as molecular linker and spacer. A combination of single-molecule force spectroscopy experiments and all-atom MD simulations in explicit water for a single molecular chain have unveiled the contribution of hydration effects to the PEG's elastic response against conformational deformations.^[41] The MD simulations revealed that entropic hydration effects almost exactly compensate the chain conformational entropy loss at high stretching. This entropic compensation was due to the stretching-induced release of water molecules that, in the relaxed state, form double hydrogen bonds with PEG.

Extending this atomistic understanding to the role of hydration in the structure and mechanics of polymer brushes

M. Ortega, J. G. Vilhena, R. Pérez
Departamento de Física Teórica de la Materia Condensada
Universidad Autónoma de Madrid
Madrid E-28049, Spain
E-mail: guilherme.vilhena@uam.es; ruben.perez@uam.es

J. G. Vilhena, R. Pérez
Condensed Matter Physics Center (IFIMAC)
Universidad Autónoma de Madrid
Madrid E-28049, Spain

 The ORCID identification number(s) for the author(s) of this article can be found under <https://doi.org/10.1002/admi.202201272>.

© 2022 The Authors. Advanced Materials Interfaces published by Wiley-VCH GmbH. This is an open access article under the terms of the Creative Commons Attribution-NonCommercial License, which permits use, distribution and reproduction in any medium, provided the original work is properly cited and is not used for commercial purposes.

DOI: 10.1002/admi.202201272

is a challenging task. First of all, we have to consider the complexity of the simulations required that involved an accurate atomistic description of the fiber–fiber and fiber–water interactions in order to capture the interplay between the hydration state and the structure of the polymer assembly that determines the collective mechanical behavior of the system. Second, we are constrained by the limited information that can be gathered from experiments regarding the structure of the system under different hydration conditions. This lack of information extends also to the energetics of system: at variance with the single fiber case, where force versus elongation curves recorded with single-molecule force spectroscopy can be directly compared with the simulations,^[41] in the case of a polymer brush, information has to be determined in a rather indirect way, for example, through the measurement of the surface stress induced in a gold-coated Si microcantilever functionalized with a densely-packed SAM of ssDNA under different hydration conditions.^[14]

In this work, we face this challenge and use MD to model the hygroscopic properties of polymer-brushes composed by ssDNA molecules. Our simulations not only provide a lively picture on how these molecular assemblies (SAM) deform under varied hydration conditions^[14,30,31] but, most importantly, they enable to identify three different swelling regimes guiding such process. We accomplish this by considering a model system where the ssDNA chains are attached to a graphene layer acting as a substrate. This choice is inspired by the use of the surface stress as a prescriptor to follow the mechanical response of a ssDNA polymer brush in the experiments^[14] discussed above. The curvature of the graphene layer provides direct access to the qualitative nature and strength of the interactions, as its low bending modulus amplifies the effects induced by hydration in this nanoscale system in order to reproduce the micro-scale experimental observations. We identify the driving mechanisms behind the dynamics revealed by the substrate curvature introducing a generalized force that captures the evolution of the different energy components of the interatomic interactions with the change in the number of water molecules in the system. This correlation between the mechanical response and the changes in the SAM structure is unveiled with the help of four averaged properties, the inter-ssDNA distance (\bar{D}), the solvent accessible area (\bar{S}_A) and the ssDNA length and width (\bar{L} and \bar{W}) that completely define the state of one of the ssDNA strands and the formation of the characteristic nanopore structure. Ultimately, it is the competition between the formation of additional water–ssDNA or water–water hydrogen bonds, in a subtle interplay with the co-evolving SAM structure, what determines the presence of three different regimes with a markedly different mechanical response.

Comparing our results for different polymer-brush densities, we demonstrate how this parameter changes the hydration onset of each of these regimes, thus explaining the aforementioned ill-behavior of ssDNA sequencing devices.^[30]

To the best of our knowledge, these results are the first to provide such multiscale picture (from hydrogen bonds up to 10 nm deformation) of a hydration-induced self-morphing nanoscale material—thus realizing the untapped

potential of MD simulations. Although based on the specific case of ssDNA, our findings that demonstrate the importance of hydration for the mechanics of SAMs and the interplay of conformational and hydration degrees of freedom are applicable to other polymer brushes and related hydrogen-bonded systems.

2. Results and Discussion

2.1. Three Different Regimes for the Mechanical Response

We consider a self-assembled monolayer of single-stranded DNA molecules tethered to a graphene substrate with a grafting density $g_d = 4 \times 10^{13} \text{ cm}^{-2}$, henceforth referred as SAM-graphene. The equilibrium configurations, obtained under different hydration conditions are shown in **Figures 1b–l**. **Figure S1** (Supporting Information) and the Experimental Section provide further details on the SAM structure and the description of our MD simulation protocol. The first and foremost result is the ability to finely regulate the mechanical deflection of the SAM-graphene by changing hydration conditions. This interplay, between hydration and mechanical deformation, may be quantified through the hydration dependence of the graphene curvature, i.e., $\chi = 1/R_{\text{curv}}$ shown in **Figure 1m** (more details in **Figure S2**, Supporting Information). There, we may differentiate three different response regimes: an ultra-low hydration one (with 0–75 water molecules per ssDNA, i.e., $H = 0 - H = 75$), where curvature remains almost constant ($\chi_{\text{not-hydrated}} \approx 0.033 \text{ nm}^{-1}$); a low hydration regime ($H = 75 - H = 100$), accompanied by a sharp curvature increase up to a maximum value of $\chi_{\text{max}} \approx 3.5 \cdot \chi_{\text{not-hydrated}}$; and finally, a hydrated regime ($H > 100$) where the curvature smoothly decreases until it saturates at $H \approx 400$ ($\chi_{\text{saturation}} \approx \chi_{\text{not-hydrated}}$).

The active role played by water molecules in mechanically deforming a much larger molecular assembly is in line with previous experiments,^[14] which exploited this phenomenon to design a label-free DNA mismatch sensor with unprecedented accuracy. Yet, lacking a physical understanding of the intricate mechanism governing its dynamics has undermined a more general use of this set-up.^[14] To compare our results with the experiments (see **Figure 1m,n**), it is important to clarify the difference between the number of water molecules (well defined in simulations) and relative humidity (controlled in experiments). In experiments, one can only estimate the number of water molecules in the chamber containing the SAM. Therefore, water molecules that are unable to desorb from the SAM do not count for the overall relative humidity measured. According to previous works,^[44,45] at 0% r.h. there are 2–3/5–6 water molecules firmly bonded to each DNA/ssDNA nucleotide. Thus, we may conservatively estimate that at 0% r.h. there are 90 water molecules available per ssDNA in our simulations (as $H = 16 \times 5.6 \approx 90$). Bearing this in mind, there is a qualitative agreement between our simulations and the experiments shown in **Figure 1m,n** for $H > 90$. This agreement sets a firm ground upon which we may now unravel the atomic origin of this complex phenomenon, and understand how solvent molecules could be used to actively modulate the mechanics of biomolecular systems.

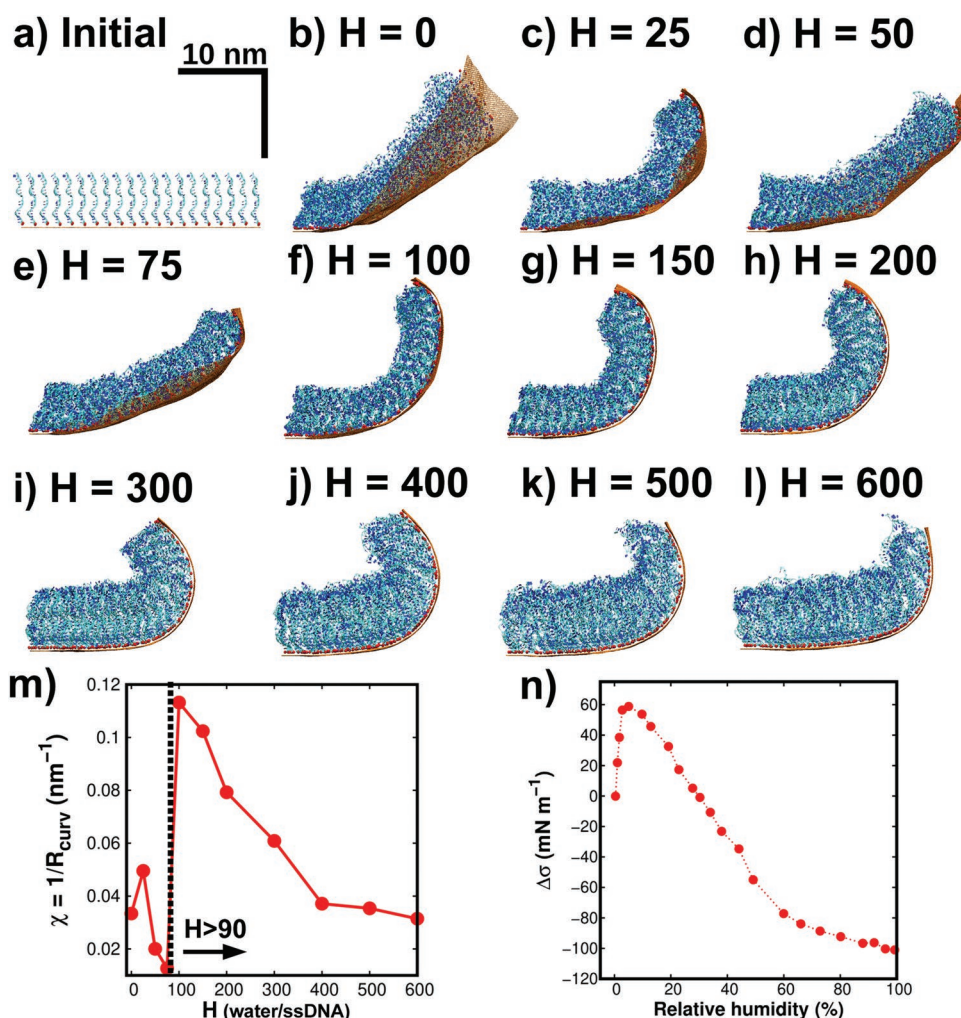


Figure 1. Water mediated mechanical deflection of a self-assembled monolayer of single-stranded DNA molecules tethered to a graphene substrate (SAM-graphene). a) Side view of the initial configuration (graphene shown in orange, ssDNA tethering points shown in red, and ssDNA represented as ribbons—further details in Methods). b–l) Equilibrium conformation of SAM-graphene obtained with different number of water molecules per ssDNA (H), i.e., hydration levels (water molecules not represented for clarity). m) Equilibrium graphene curvature, i.e. $\chi = 1/R_{\text{curv}}$, as a function of the hydration level (see Figure S2, Supporting Information, for details). n) Experimentally reported^[14] surface stress as a function of relative humidity computed from surface curvature using Stoney's equation^[42,43] (i.e. $\sigma \propto \chi$).

2.2. Driving Mechanisms: Generalized Forces and Hydrogen Bonding

The dynamics of the SAM-graphene at different hydration conditions can be understood in light of the six energy components defining all inter-atomic interactions (see Figure 2a), namely: the graphene internal energy (E^G), the ssDNA energy (E^D), the water energy (E^W), the water-ssDNAs interaction energy (E^{W-D}), the graphene-ssDNAs interaction energy (E^{G-D}) and the water-graphene interaction energy (E^{W-G}). We are interested in understanding how these energy contributions change with hydration. To this end, we consider the virtual work exerted by all atoms associated with a small perturbation of the system:

$$\begin{aligned} W &= dE^G + dE^D + dE^W + dE^{W-D} + dE^{G-D} + dE^{W-G} \\ &= \sum_{i,j} \frac{dE^i}{dH} \cdot \frac{dH}{d\mathbf{r}_j} \cdot d\mathbf{r}_j \end{aligned} \quad (1)$$

where \mathbf{r}_j are the cartesian coordinates of the atoms and H is a generalized coordinate (as the ones introduced in the context of Lagrangian mechanics) representing the change in hydration. From Figure 2a, we observe that only E^D , E^W and E^{W-D} change with the hydration level, from what it follows:

$$dW \approx Q_H^D dH + Q_H^W dH + Q_H^{W-D} dH \quad (2)$$

being $Q_H^i = \frac{dE^i}{dH}$ the corresponding generalized force associated to H in Lagrangian mechanics. Note that although this generalized force doesn't have force dimensions (not a necessity for a Lagrangian generalized force), the product $Q_H^i dH$ has dimensions of work/energy. This generalized force, may be understood as a hydration driving force, whereby a positive/negative value indicates whether increasing the number of water molecules in the system favors (counters) the mechanical deflection by increasing (reducing) the system total energy. Although

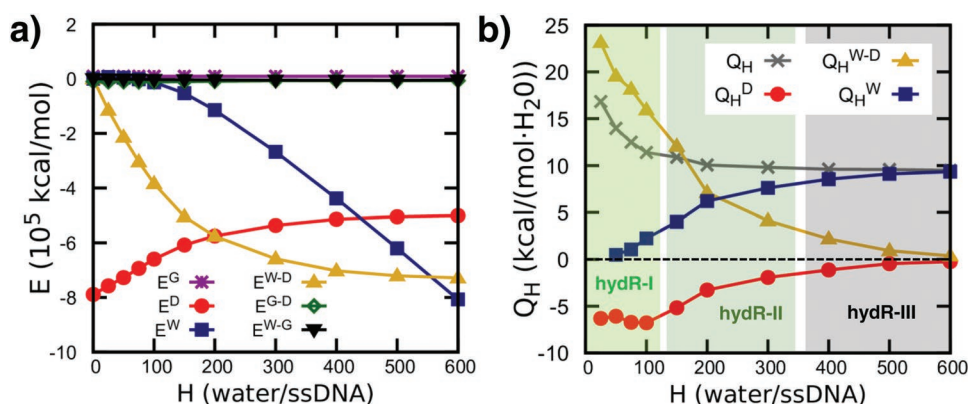


Figure 2. Driving mechanisms of hydration that induced mechanical deflection. a) Hydration dependence of the six energy components governing SAM-graphene dynamics, i.e., graphene internal energy (E^G), ssDNAs energy (E^D), water energy (E^W), water-ssDNAs interaction (E^{W-D}), graphene-ssDNAs interaction (E^{G-D}) and water-graphene interaction (E^{W-G}). b) Generalized force as a function of hydration ($Q_H = -\Delta E(H)/(200 \cdot \Delta H)$, being $E(H)$ the energy at hydration H) computed from: the total energy (Q_H), ssDNAs energy (Q_H^D), water energy (Q_H^W), and the water-ssDNAs interaction (Q_H^{W-D}). The shaded areas in b) delimit the three distinct hydration regimes.

related, this generalized force differs from the common definition of hydration force.^[46,47]

These generalized forces are calculated as:

$$Q_H^i(H_j) = -\frac{\Delta E^i}{\Delta N_{H_2O}} = -\frac{E(H_j) - E(H_{j-1})}{200 \cdot (H_j - H_{j-1})} \quad (3)$$

where N_{H_2O} is the total number of water molecules in the system (i.e. $200 \times H_j$), and $E^i(H_j)$ is the energy (total or a component) at a given hydration H_j .

Figure 2b displays the total generalized force (Q_H) and its three major components, i.e., the contribution from the change of water internal energy (Q_H^W computed from E^W), the contribution from the interaction of the ssDNA molecules (Q_H^D), and the water-ssDNAs interaction (Q_H^{W-D}). Q_H is positive for all the hydrations, trivially confirming that deformation with increasing number of water molecules is an energetically favorable process. However, only Q_H^{W-D} and Q_H^W remain positive for all considered hydration values, thus being the sole net contributors of the SAM deformation. Additionally, we observe that they evolve differently with increasing number of water molecules: Q_H^{W-D} decreases whereas Q_H^W increases. Thus, on the one hand, at $H=0$, the water-ssDNA generalized force contribution is much larger than the water-water one ($|Q_H^{W-D}| > 6 \times |Q_H^W|$). While, on the other hand, for high hydration values $|Q_H^{W-D}| \sim 0$ whereas $|Q_H^W|$ steadily increases nearly reaching $10 \text{ kcal (mol} \times H_2O)^{-1}$. This shows that the dominant driving mechanism changes with hydration level. In particular, at low hydration, the formation of more water-ssDNA hydrogen bonds is favored, whereas at high hydration, the formation of new water-water hydrogen bonds prevails (hereafter referred as h-bonds). Consequently, we may define three hydration regimes (hydR), differentiated by the physical mechanisms which contribute the most towards the SAM-graphene deformation (see shadowed regions in Figure 2b). First, when $H \leq 100$ (hydR-I), $|Q_H^{W-D}|/|Q_H^W| > 6$ and thus the formation of new water-ssDNA h-bonds is the main driving mechanism. Second, in the $100 < H < 400$ range (hydR-II), $0.5 \leq |Q_H^{W-D}|/|Q_H^W| < 2.5$ and, so, the driving mechanism arises from a combination of both the water-ssDNA interaction (formation of

new water-ssDNA h-bonds) and the water-water interaction (formation of new water-water h-bonds). Finally, for $H \geq 400$ (hydR-III), $|Q_H^{W-D}|/|Q_H^W| < 0.5$, showing that the main driving-deformation process is the formation of new water-water h-bonds. In what follows, we provide an atomically detailed picture of the SAM-graphene structure in these three different hydration regimes and show how it contributes to determine the mechanical response.

2.3. Low Hydration Regime

In the hydR-I ($0 < H \leq 100$) the driving mechanism of the SAM-graphene deflection is the high water-ssDNAs affinity, ultimately powered by the formation of new water-ssDNA h-bonds.^[48,49] Figure S3 (Supporting Information) shows that, in this first regime, the number of h-bonds formed between one water molecule and a single atom in a ssDNA molecule, ($N_{\text{single h-bonds}}$), linearly increases with hydration, highlighting that the probability of forming this type of h-bond does not decrease with hydration. In fact, $N_{\text{single h-bonds}}/N_{H_2O} = N_{\text{single h-bonds}}/(H \times 200) \approx 0.5$, showing that one single h-bond is formed per each two water molecules added to the system during the whole regime. More importantly, the number of water-ssDNA h-bonds formed between a single water molecule and two different atoms in ssDNA, (h-bridges), grows very rapidly with hydration in this regime (see Figure 3a.) This results from an increase of both the number of intra h-bridges (a bond formed between one water molecule and two atoms belonging to the same ssDNA strand) and the number of inter h-bridges (where the atoms belong to two different ssDNA strands), as shown in Figure 3a.

The structural modifications arising from the enhanced water-ssDNA h-bond formation are the best understood in light of four SAM structural properties: the inter-ssDNA distance (\bar{D} , in Figure 3b), the ssDNAs solvent accessible area (\bar{S}_A , in Figure 3c), and the ssDNAs length and width (respectively \bar{L} and \bar{W} in Figure 3d). From this analysis, we can distinguish two predominant structural changes suffered by the SAM

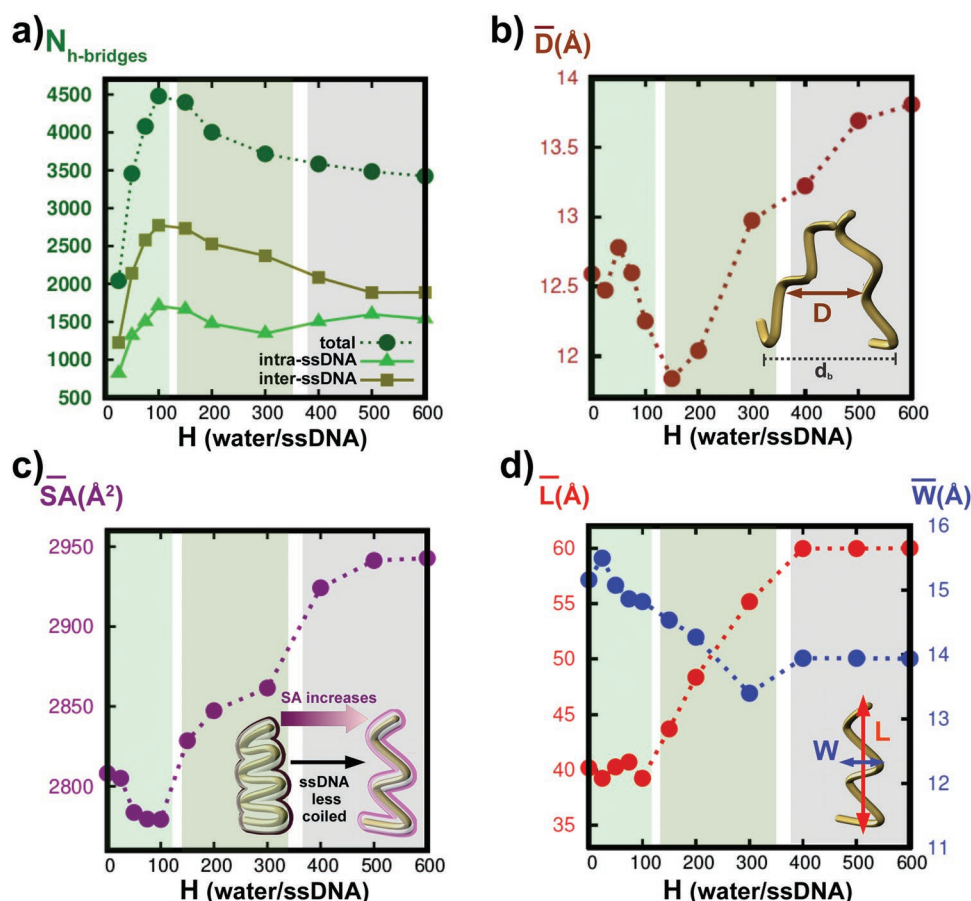


Figure 3. SAM structural evolution during hydration process. a) Number of h-bridges ($N_{h\text{-bridges}}$) as a function of hydration. Here we distinguish: total number, the ones formed between atoms of a same ssDNA strand (intra-ssDNA), and the ones formed between atoms of two different ssDNA strands (inter-ssDNA). Further details in Methods section. Evolution during hydration process of the: b) inter-strand distance (\bar{D}), c) ssDNAs solvent accessible area (\bar{SA}), d) ssDNAs length (\bar{L}) and width (\bar{W}). A schematic representation of the definition of each magnitude is included as an inset in the respective figure. The represented values were computed by averaging the instantaneous data obtained in the last 10 ns of simulation for all the ssDNA molecules. In all figures the three hydration regimes are delimited with shaded areas (see Figure 2).

during the hydr-I range. First, we observe that $\bar{D} \approx 12.5 \text{ \AA}$ when the system is not hydrated and this barely changes during the first regime (Figure 3b). Considering that the bottommost ssDNA atoms are restrained at a distance of $d_b \approx 15.8 \text{ \AA}$, this shows that adjacent ssDNAs coalesce and are unable to separate during the first hydration regime (Figure 3b). Second, \bar{SA} decreases during the hydr-I regime. Considering the relation between \bar{SA} and the grade of compactness of a single ssDNA, -see the schematic representation in the inset of Figure 3c-, this decrease implies that the ssDNAs are becoming more compact/coiled with increasing hydration. These two structural changes are consistent with the main driving mechanism of the SAM-graphene movement during the hydr-I regime: the formation of water-ssDNA single h-bonds and h-bridges. As schematically represented in Figure 4a, adjacent ssDNAs need to approach each other for enabling the possibility to form inter h-bridges. This coalesce of ssDNA molecules gives rise to the upward deflection of the SAM-graphene system. Moreover, the more coiled the ssDNA structure, the larger the number of ssDNA areas that enable the formation of both intra h-bridges and inter h-bridges, see Figure 4a. Both effects lead to a reduction

of the mobility of each ssDNA, making the whole structure stiffer. This explains the enhancement of the SAM-graphene mechanical response observed in Figure 1m during this hydr-I regime.

As shown in Figure 1m, the SAM-graphene hydro-mechanical response is not a gradual process. Following the initial ($H < 75$) state of almost constant curvature, we observe a sudden increase for hydration levels in the range of $75 < H < 100$. In contrast with this global property, at the single strand level, we observe that changes progress smoothly in this hydration range. This is particularly notorious with the smooth increase (decrease) of $N_{h\text{-bridges}}$ (\bar{SA}) shown in Figure 3a,c. The spatial standard deviation of \bar{D} ($\sigma(D)$), and the water molecule distribution along the SAM for $H = 25\text{--}100$ (see Figures S4 and S5, Supporting Information, for more details) helps us to rationalize the different character of the global and local deformations. Although $\sigma(D)$ barely changes from $H = 0$ to $H = 75$, it significantly decreases between $H = 75$ and $H = 100$, thus showing a hydration-induced heterogeneous to homogeneous transition. Interestingly, the water distribution in the SAM undergoes

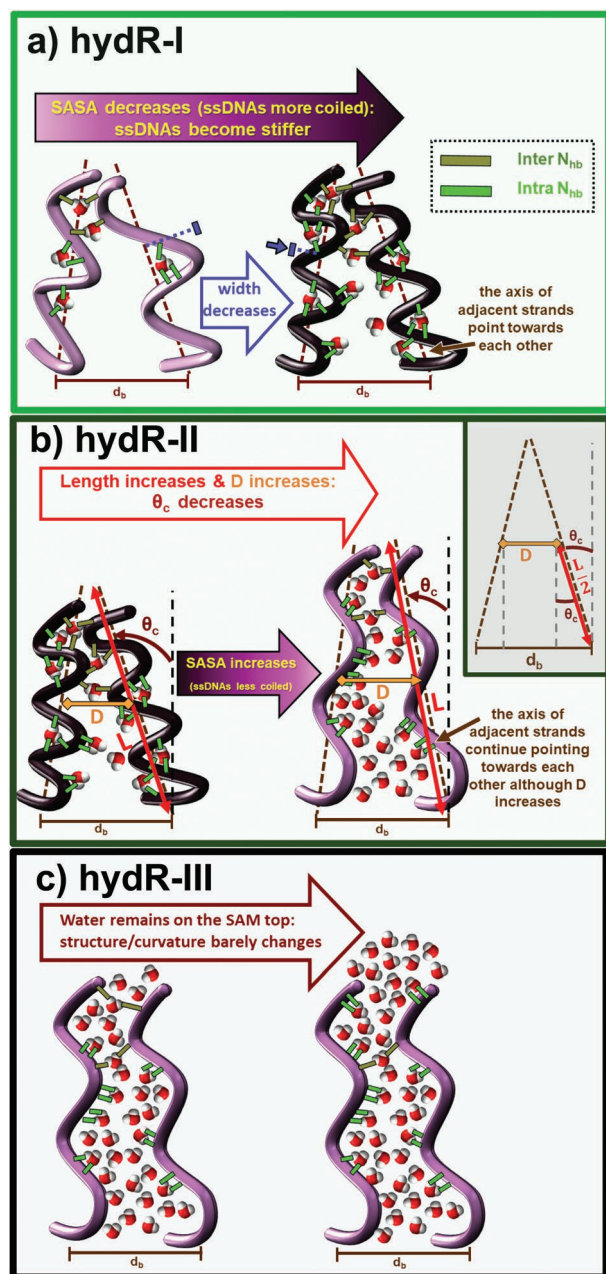


Figure 4. Schematic representation of the main SAM structural changes occurring on the a) hydr-I, b) hydr-II and c) hydr-III ranges. The ssDNAs are schematically represented as helical-shaped molecules coloured with pink shades according to their $\bar{S}A$ evolution, i.e., the brighter the ssDNAs are coloured, the larger their $\bar{S}A$ value is (they are less coiled). The water atoms are schematically represented as van-der-Waals spheres coloured according to their atom type (oxygen atom in red, hydrogen atoms in white). The evolution of the number of intra h-bridges/inter h-bridges on each hydration range is here schematically represented via the green/ochre lines connecting the water molecules with the ssDNA strands. The evolution of $\bar{L}/\bar{W}/\bar{D}$ on each hydration range is also here indicated with red/blue/orange arrows. The relation of the ssDNAs curvature angle (θ_c) with \bar{D} and \bar{L} is schematically represented on the inset.

a similar transition, being unevenly distributed for $H < 75$ and remarkably homogeneous at $H = 100$. The heterogeneity at low hydration ($H < 75$) in both strand distance and water

distribution ultimately results in an absence of a significant collective motion of the SAM in this range. ssDNAs move in different directions so their individual contributions to the SAM mechanical response do not sum up efficiently. Thus, a global property such as the SAM-graphene curvature barely increases (see Figure 1m). On the contrary, when the SAM homogeneity increases (for $H = 75$ –100), the ssDNAs start to cooperatively work in the same direction, leading to a sharp increase of the SAM-graphene curvature.

2.4. Mid-Hydration Regime

In the hydr-II regime ($100 < H < 400$), $N_{\text{single h-bonds}}$ continues increasing with the hydration but $N_{\text{single h-bonds}}/H$ starts to decrease (Figure S3, Supporting Information). This last result highlights that the probability of forming new water–ssDNA single h-bonds decreases during the hydr-II, in contrast with the results observed in the previous regime. Furthermore, $N_{\text{h-bridges}}$ also decreases from $H > 100$ to $H = 400$ (Figure 3a), signaling the continuous breaking of intra h-bridges and inter h-bridges as the hydration raises. All in all, these results are in agreement with the progressive decrease of the water–ssDNA affinity which characterizes the hydr-II regime accordingly to the Q_H^{W-D} evolution (Figure 2b). Additionally, they imply that maintaining all water–ssDNA h-bridges formed in the hydr-I range is no longer a driving mechanism for $H > 100$, and, thus, the SAM structure has to significantly change for enabling some of these h-bridges to be broken. That significant change can be seen in \bar{L} , that increases up to 50% from $H > 100$ to $H = 400$ (Figure 3d). This is accompanied by a substantial $\bar{S}A$ increment and a \bar{W} decrease (Figure 3c,d). Therefore, in this regime, the addition of new water molecules to the system stretches the ssDNA molecules, causing them to narrow over the SAM and to become less coiled (Figure 4b). These structural changes, consistent with the breaking of h-bridges (Figure 4b), enlarge the free space between two adjacent ssDNAs, favoring the formation of nanopores. The growth of well defined nanopores, that can accommodate a larger number of water molecules, favors the water–water interaction. This result is consistent with the emergence of the water energy (E^W) as the new driving agent of the system (Figure 2b).

The SAM structural variations occurring during this hydr-II regime allow us to understand the decrease of the SAM-graphene curvature observed from $H > 100$ to $H = 400$ (Figure 1m). First, the ssDNAs substantially stretch ($\approx 50\%$) during the hydr-II range (Figure 3d). Second, \bar{D} increases $\approx 11\%$ from $H = 150$ to $H = 400$ (Figure 3b), highlighting that adjacent ssDNAs progressively separate from each other. Third, $\bar{D} < d_b \approx 15.8 \text{ \AA}$ during the whole hydr-II range indicating that the axis of adjacent strands continue pointing towards each other despite their separation (Figure 4a,b). These three structural changes directly affect the mean curvature angle of each ssDNA on the SAM—a magnitude hereafter refereed as θ_c that is related with \bar{L} and \bar{D} as (see Figure 4b):

$$\sin \theta_c \sim \theta_c \sim \frac{(d_b - \bar{D})/2}{\bar{L}/2} = \frac{d_b}{\bar{L}} - \frac{\bar{D}}{\bar{L}} \quad (4)$$

Therefore, as predicted by Equation (4), the increase of both \bar{L} and \bar{D} from $H > 100$ to $H = 400$ prompts the continuous decrease of θ_c . This explains the progressive reduction of the SAM-graphene general curvature observed during the hydr-II (Figure 1m). This reduction in the mechanical response has been previously attributed exclusively to a water-mediated repulsive ssDNA interaction.^[14] Our results clearly show that changes in the SAM structure, associated to the strong variation of the ssDNAs conformation and length, play a key role.

2.5. High Hydration Regime

Finally, in the hydr-III regime ($400 \leq H \leq 600$), $N_{\text{h-bridges}}$ and $N_{\text{single h-bonds}}$ saturate as shown in Figure 3a and Figure S3 (Supporting Information). Changing the number of water-ssDNA h-bonds is no longer an effective driving mechanism, as quantified by the negligible $Q_{\text{H}}^{\text{W-D}}$ characterizing this regime (Figure 2b). Consequently, adding new water molecules no longer influences the ssDNAs structure. This is evidenced by the saturation of its structural parameters ($\bar{D}, \bar{L}, \bar{S}, \bar{W}$) from $H = 400$ to $H = 600$ (Figure 3b–d). Our simulations show that, as the system hydrates, new water-water h-bonds within the SAM nanopores becomes less and less favourable and water molecules position instead on top of the (see Figure S6, Supporting Information, for $H > 400$). Thus, although hydration is still energetically favourable (see E^{W} evolution in Figure 2a), it barely affects the SAM structure. This is consistent with the results observed in Figure 3a–d for the hydr-III range, and explains the saturation of the SAM-graphene curvature evolution for $H > 400$, see Figure 1m.

2.6. The Role of Polymer Density

One of the major issues hampering a more widespread use of ssDNA brushes is the fact that their properties depend on grafting density in a uncontrolled/unknown manner. DNA sequencing devices^[14,30,31] are a good example. Based on the accurate description attained by MD at high densities (Figure 1), we now explore the low density regime. We followed exactly the same simulation/analysis procedure described above but on a ssDNA SAM with a lower grafting density ($g_d = 3 \times 10^{13}$ molecules cm^{-2}). For this density, the separation between the bottommost position of adjacent strands is larger ($d_b = 18$ Å, see more details on the Supporting Information). Figure S7 (Supporting Information) shows the hydration-induced mechanical changes predicted by MD for this second SAM—henceforth referred as sparser-SAM. The curvature of the sparser-SAM continuously increases when $H < 75$, while it sharply decreases for $75 < H < 100$. This is a markedly distinct behavior from the denser SAM (Figure 1). These findings explain prior experiments in DNA sequencing devices,^[31] and evidence how the grafting density can substantially alter hydration-induced mechanical response of these brushes.

To understand the role of the grafting density, we turn to an analysis of both structural and enthalpic properties of the sparser-SAM. Figure S8 (Supporting Information) shows that \bar{L} decreases in the $H = 0$ –75 range and increases when $H > 75$.

Two main conclusions follow from this evolution. First, \bar{L} evolution at low hydration ($H = 0$ –100) changes significantly when the grafting density is reduced: at the higher grafting density, \bar{L} remained virtually constant, while it clearly decreases in the case of the smaller grafting density (Figure S8a, Supporting Information). Second, the \bar{L} – H evolution for the two grafting densities is compatible with the mechanisms governing the mechanical deflection, as a general decrease (increase) of the ssDNAs length will increase (decrease) the system curvature, see Figure 4b and Equation (4).

The \bar{L} hydration dependence for the varied grafting densities is best understood in conjunction with \bar{W} (Figure S8a, Supporting Information). For compact grafting, $\bar{W}_{H=0} \approx d_b = 15.5$ Å, i.e. all space between adjacent ssDNAs is essentially filled with its own atoms. Consequently, ssDNAs need to become narrower in order to allow water entering into the nanopores. However, for the sparser-SAM, $\bar{W}_{H=0} < d_b = 18$ Å, i.e. the free volume between two adjacent ssDNAs (nanopore) at $H = 0$ is already large enough for water molecules to enter. Thus, instead of compacting, ssDNAs broaden their structure, allowing a larger ssDNA–water–ssDNA interaction inside the nanopores and increasing inter h-bridges (Figure S8b, Supporting Information). This broadening naturally results in less coiled (see \bar{S} evolution in Figure S8a) and shorter ssDNAs, explaining the \bar{L} (χ) decrease (increase) observed for $H < 75$ (see Figures S7 and S6, Supporting Information). However, when the number of water molecules is large enough to fill the volume of the nanopores ($H > 50$), ssDNAs start to compact (\bar{W} decreases with the hydration), allowing more water molecules to enter the nanopores and promoting the increase (decrease) of \bar{L} (χ) for $H > 75$.

The grafting density influence is also apparent on the driving mechanisms. As shown in Figure S8c (Supporting Information), for the sparser-SAM, the evolution with the hydration of the three major components of the generalized force (Q_{H}^{D} , $Q_{\text{H}}^{\text{W-D}}$ and Q_{H}^{W}) is similar to the one obtained for the compact SAM. This similarity is particularly notorious at low hydration levels ($H = 0$ –100). Therefore, the structural/mechanical changes resulting from a different grafting density do not have an enthalpic origin, leaving only entropic configurational effects as the main mechanism leading to the different mechanical response. This idea is further reinforced by the characterization of the SAM homogeneity degree at low hydration levels for both grafting density values (Figures S8d and S9, Supporting Information). The reduction of the grafting density increases the range of possible intra-ssDNA distances found along the SAM when the hydration is low ($H = 0$ –100), i.e., the SAM becomes less homogeneous. Consequently, a larger entropic contribution is expected on the sparser-SAM. Therefore, sparser-SAM results highlight the importance of considering entropic effects to obtain a complete description and understanding of the behaviour of these ssDNA assemblies.^[30,34]

3. Conclusions

To conclude, our results provide a unprecedented atomically resolved understanding of hygroscopic properties of polymer-brushes and how the picosecond dynamics of hydrogen bonds relates to hundreds of nanosecond long deformations

propagating through several nanometers, -i.e., a portrait of this inherently multiscale process-. Importantly, we identify three different swelling/deformation regimes of ssDNA nano-brushes. Their mechanical response depends significantly on the grafting density. These results rationalize several difficulties related to the use of such brushes in DNA sequencing devices^[14,31] (such as initial preparation conditions), and are also relevant to guide the design of other polymer-brush based smart materials.^[18] Finally, provided the extreme hygroscopic power of ssDNA brushes (capable of absorbing 80% of its mass in water, thus doubling the common silica-gel desiccants) our work paves the way for an alternative design of hygroscopic materials based on biological polymers such as single-stranded DNA molecules.

4. Experimental Section

System Preparation and Force Fields: The SAMs studied in this work were constituted by 200 ssDNA strands distributed with a quadrangular packing configuration in a rectangle of 20×10 molecules (Figure S10a, Supporting Information). Rectangular SAMs were used to mimic the ones experimentally studied on refs. [14,31], i.e., ssDNA strands immobilized in rectangular micro-cantilevers. The ssDNA molecule consisted of an stretched A-form single-strand with the same sequence as in the experimental results reported in refs. [14,31], i.e., 5'-CTACCTTTTTTCTG-3'. Two different grafting density values (g_d) were inspected, which were determined by fixing the distance between the bottom-most positions (C5' atom of last nucleotide) of adjacent strands, i.e., d_b ($d_b \sim 15.8/18$ Å when $g_d = 4/3 \times 10^{13}$ cm⁻²; Figure S10b, Supporting Information). Once the SAMs were prepared, each of them was centred on top of a one-layer graphene with dimensions $30 \times 15.6/35 \times 17.5$ nm² when $g_d = 4/3 \times 10^{13}$ cm⁻². The initial distance between the bottommost atom of all the ssDNA strands and the graphene layer was ≈ 3.5 Å. Given that the phosphate groups in the backbone of the ssDNA were charged, to achieve charge neutrality 15 sodium counter-ions were added per each ssDNA molecule.

The parmbsc0^[50] modification of the Cornell ff99 force field^[51] was used for the ssDNAs. This force field was known to properly describe DNA's hydration,^[52,53] mechanical,^[54] and frictional^[55] properties, as well as its behavior in DNA self-assembled monolayers.^[30] The graphene atoms were modeled using the OPLS aromatic carbon force field included in the AMBER generalized force field.^[56] This force field properly described graphene mechanical and hydration properties^[57,58] as well as its interaction with biological systems^[59,60] such as DNA/ssDNA.^[61–63]

The sodium counterions were described using the Joung/Cheatham parameters.^[64] The water molecules were described using the Explicit TIP3P water model.^[65] This water model suitably described the DNA hydration pattern^[53] and also graphene's wetting properties.^[66]

MD Parameters and Simulation Protocol: The AMBER14 software suite^[67] with NVIDIA GPU acceleration was used.^[68,69] For the sake of numerical efficiency and accuracy, periodic boundary conditions were used with a rectangular box that extends >70 Å above/beyond the whole system in the x and z directions. To restrict the system movement in the y direction (see Figure S10a, Supporting Information), the box size in that direction to the system size was fitted, i.e., $158.1/180$ Å when $g_d = 4/3 \times 10^{13}$ cm⁻². To account for long-range electrostatic interactions, Particle Mesh Ewald^[70,71] was used with a real-space cutoff of 10 Å. Van-der-Waals interactions were also truncated at the real-space cutoff. An integration time step of 1 fs was used and coordinates were saved every 1000 steps. A constant temperature of 300 K was ensured in all the simulations by means of a Langevin thermostat.^[72] Our simulation protocol is composed by three main stages. In the first stage, an energy minimization was performed to prevent steric clashes, using a combination of steepest descent and conjugate gradient methods. During this process, restraints were kept at all the ssDNA atoms and the

graphene monolayer. In the second stage, the system from 0 to 300 K using a 1 ns long NVT simulation while restraining again the position of all the ssDNA and graphene atoms was heated up. Finally, a 180 ns long Steered Molecular Dynamics (SMD) simulation was performed to analyze the system mechanical behavior. That simulation was based on two main characteristics. First, the position of the left-most graphene atoms forcing the system to deflect in one direction (Figure S10a) was kept fix. Second, the distance between the bottommost atom of all the ssDNA molecules (C5' of the last nucleotide) and its nearer graphene atom to ≈ 3.5 Å via an harmonic restrain ($k = 100$ kcal mol⁻¹) was restrained, see Figure S10a (Supporting Information). That restrain was maintained during the whole dynamic, allowing that the distance between the ssDNAs bottom-part and the graphene layer hardly changes during the simulation. Thus, the dynamic of the graphene substrate was not restricted, but the ssDNAs were always fixed to it (see Figure S10a, Supporting Information). This simulation protocol was performed for the SAM with $g_d = 4 \times 10^{13}$ cm⁻² using eleven different hydration levels (H) defined accordingly to the number of water molecules per ssDNA included on the system: $H = 0, 25, 50, 75, 100, 150, 200, 300, 400, 500$, and 600 . For all these cases, it was found that at the end of the simulation both the structural parameters and the total energy of the system were fully converged, see Figure S11 (Supporting Information). When $g_d = 3 \times 10^{13}$ cm⁻², this simulation protocol was only performed for low hydration levels ($H = 0-300$), as it was observed that the major differences were obtained in that hydration range (see Figure S8, Supporting Information).

Data Analysis: The time-evolution of the six energy components of the system total energy ($E^G, E^D, E^W, E^{W-D}, E^{G-D}, E^{W-G}$) was obtained by performing an energy decomposition on each recorded frame of the MD trajectories. The three interaction energies, i.e., E^{W-D}, E^{W-G} and E^{G-D} were defined as (E^{W-D} as an example was used):

$$E^{W-D}(t) = E^{W+D}(t) - E^W(t) - E^D(t) \quad (5)$$

where E^{W+D} stands for the energy of the combined water+ssDNAs system. The values represented in Figure 2a corresponds with a time average of the obtained data for each energy component in the last 10 ns, i.e. when the system is thermally equilibrated (see Figure S11, Supporting Information).

Moreover, the CPPTRAJ tools within the AMBER package^[73] were used to characterize the SAM structure at each hydration level. For obtaining ssDNAs length and width (L and W respectively, see definition on Figure S10b, Supporting Information), the radius of gyration tensor (Rg) of each ssDNA was calculated.^[73] Thus, L/W was estimated through the Rg component that was parallel/perpendicular to each ssDNA axis. The distance between adjacent ssDNAs (D, see Figure S10b, Supporting Information) was computed for all pairs of adjacent strands along the x direction and was defined as the distance between the ssDNAs axes (see Figure S10b, Supporting Information).^[73] Finally, the solvent-accessible surface area of each ssDNA^[73,74] for estimating its grade of compactness (see Figure 3) was computed. Additionally, the relation between the water molecules and the ssDNAs structure was analyzed by calculating the number of h-bonds formed between one water molecule and one ssDNA atom ($N_{\text{single h-bonds}}$),^[73] and the number of h-bonds formed between one water molecule and two ssDNA atoms ($N_{\text{h-bridges}}$).^[73] L, W, D, and SA were calculated for all the ssDNAs. Then, their spatial-average along the SAM and their spatial standard deviation were computed (\bar{X} and σX with $X = L, W, SA, D$). The spatial-average and spatial standard deviation of these four structural magnitudes (L, W, D, and SA) together with $N_{\text{single h-bonds}}$ and $N_{\text{h-bridges}}$ were evaluated each 20 ps during the last 10 ns of the MD trajectories (the system is thermally equilibrated, see Figure S11, Supporting Information), and time-averaged in that time slot for studying their evolution with the hydration level (see results on Figure 3).

Supporting Information

Supporting Information is available from the Wiley Online Library or from the author.

Acknowledgements

The authors thank the Spanish MINECO for financial support (project MAT2017-83273-R). J.G.V. and R.P. acknowledge support from the Spanish Ministry of Science and Innovation, through project PID2020-115864RB-I00 and the “María de Maeztu” Programme for Units of Excellence in R&D (CEX2018-000805-M). J.G.V. acknowledge support from the Spanish Ministry of Science and Innovation (PID2020-113722RJ-I00) and Spanish CM “Talento Program” Project No. 2020-T1/ND-20306.

Conflict of Interest

The authors declare no conflict of interest.

Data Availability Statement

The data that support the findings of this study are available from the corresponding author upon reasonable request.

Keywords

hydration, hygroscopic properties, mechanical responses, molecular dynamics, ssDNA polymer brushes

Received: June 7, 2022

Revised: September 5, 2022

Published online: October 17, 2022

- [1] J. Carrasco, A. Hodgson, A. Michaelides, *Nat. Mater.* **2012**, *11*, 667.
- [2] D. Martín-Jiménez, E. Chacón, P. Tarazona, R. García, *Nat. Commun.* **2016**, *7*, 12164.
- [3] D. Martín-Jiménez, R. García, *J. Phys. Chem. Lett.* **2017**, *8*, 5707.
- [4] M. Ricci, P. Spijker, K. Voitchovsky, *Nat. Commun.* **2014**, *5*, 4400.
- [5] K. Voitchovsky, M. Ricci, in *Colloidal Nanocrystals for Biomedical Applications VII*, (Eds. W. J. Parak, K. Y. M. D., M. Osinski), vol. 8232, International Society for Optics and Photonics, SPIE, Bellingham, WA **2012**, pp. 120–127, <https://doi.org/10.1117/12.905864>.
- [6] H. R. Corti, G. A. Appignanesi, M. C. Barbosa, J. R. Bordin, C. Calero, G. Camisasca, M. D. Elola, G. Franzese, P. Gallo, A. Hassanali, K. Huang, D. Laria, C. A. Menéndez, J. M. M. de Oca, M. P. Longinotti, J. Rodríguez, M. Rovere, D. Scherlis, I. Szleifer, *The European Physical Journal E* **2021**, *44*, 136.
- [7] K. Falk, F. Sedlmeier, L. Joly, R. R. Netz, L. Bocquet, *Nano Lett.* **2010**, *10*, 4067.
- [8] D. Ortiz-Young, H.-C. Chiu, S. Kim, K. Voitchovsky, E. Riedo, *Nat. Commun.* **2013**, *4*, 2482.
- [9] C. Sendner, D. Horinek, L. Bocquet, R. R. Netz, *Langmuir* **2009**, *25*, 10768.
- [10] D. M. Huang, C. Sendner, D. Horinek, R. R. Netz, L. Bocquet, *Phys. Rev. Lett.* **2008**, *101*, 226101.
- [11] F. Martelli, C. Calero, G. Franzese, *Biointerphases* **2021**, *16*, 020801.
- [12] F. Leoni, C. Calero, G. Franzese, *ACS Nano* **2021**, *15*, 19864.
- [13] C. Calero, G. Franzese, *J. Mol. Liq.* **2020**, *317*, 114027.
- [14] J. Mertens, C. Rogero, M. Calleja, D. Ramos, J. A. Martín-Gago, C. Briones, J. Tamayo, *Nat. Nanotechnol.* **2008**, *3*, 301.
- [15] S. Ciampi, N. Darwish, H. M. Aitken, I. Díez-Pérez, M. L. Coote, *Chem. Soc. Rev.* **2018**, *47*, 5146.
- [16] J. G. Vilhena, C. Pimentel, P. Pedraz, F. Luo, P. A. Serena, C. M. Pina, E. Gnecco, R. Pérez, *ACS Nano* **2016**, *10*, 4288.
- [17] M. Ortega, J. G. Vilhena, P. Rubio-Pereda, P. A. Serena, R. Pérez, *J. Chem. Theory Comput.* **2019**, *15*, 2548.
- [18] H. Quan, D. Kisailus, M. A. Meyers, *Nat. Rev. Mater.* **2021**, *6*, 264.
- [19] X. Zhang, L. Chen, K. H. Lim, S. Gonuguntla, K. W. Lim, D. Pranantyo, W. P. Yong, W. J. T. Yam, Z. Low, W. J. Teo, H. P. Nien, Q. W. Loh, S. Soh, *Adv. Mater.* **2019**, *31*, 1804540.
- [20] K. Oliver, A. Seddon, R. S. Trask, *J. Mater. Sci.* **2016**, *51*, 10663.
- [21] R. M. Erb, J. S. Sander, R. Grisch, A. R. Studart, *Nat. Commun.* **2013**, *4*, 1712.
- [22] S. A. Maynard, A. Gelmi, S. C. Skaalure, I. J. Pence, C. Lee-Reeves, J. E. Sero, T. E. Whittaker, M. M. Stevens, *ACS Nano* **2020**, *14*, 17321.
- [23] E. Kim, S. Agarwal, N. Kim, F. S. Hage, V. Leonardo, A. Gelmi, M. M. Stevens, *ACS Nano* **2019**, *13*, 2888.
- [24] Y. Han, J. Hu, X. Chen, *Mater. Chem. Front.* **2019**, *3*, 1128.
- [25] Y. Wu, D. U. Shah, B. Wang, J. Liu, X. Ren, M. H. Ramage, O. A. Scherman, *Adv. Mater.* **2018**, *30*, 1707169.
- [26] C. Huang, D. Quinn, S. Suresh, K. J. Hsia, *Proceedings of the National Academy of Sciences* **2018**, *115*, 70.
- [27] Q. Zhao, J. W. Dunlop, X. Qiu, F. Huang, Z. Zhang, J. Heyda, J. Dzubiella, M. Antonietti, J. Yuan, *Nat. Commun.* **2014**, *5*, 1.
- [28] C. Dawson, J. F. Vincent, A.-M. Rocca, *Nature* **1997**, *390*, 668.
- [29] S. Armon, E. Efrati, R. Kupferman, E. Sharon, *Science* **2011**, *333*, 1726.
- [30] C. M. Domínguez, D. Ramos, J. I. Mendieta-Moreno, J. L. G. Fierro, J. Mendieta, J. Tamayo, M. Calleja, *Sci. Rep.* **2017**, *7*, 536.
- [31] C. M. Domínguez, P. M. Kosaka, G. Mokry, V. Pini, O. Malvar, M. del Rey, D. Ramos, Á. San Paulo, J. Tamayo, M. Calleja, *Langmuir* **2014**, *30*, 10962.
- [32] J. Fritz, M. K. Baller, H. P. Lang, H. Rothuizen, P. Vettiger, E. Meyer, H. J. Güntherodt, C. Gerber, J. K. Gimzewski, *Science* **2000**, *288*, 316.
- [33] R. McKendry, J. Zhang, Y. Arntz, T. Strunz, M. Hegner, H. P. Lang, M. K. Baller, U. Certa, E. Meyer, H.-J. Güntherodt, C. Gerber, *Proceedings of the National Academy of Sciences* **2002**, *99*, 9783.
- [34] N. Zhang, Z. Tan, J. Li, W. Meng, L. Xu, *Current Opinion in Colloid and Interface Science* **2011**, *16*, 592.
- [35] Z. Xin-Jun, G. Zhi-Fu, J. Zhong-Ying, *Chin. Phys. B* **2015**, *24*, 044701.
- [36] M. Wagman, S. Medalion, Y. Rabin, *Macromolecules* **2012**, *45*, 9517.
- [37] S. Pal, B. C. Ray, *Molecular Dynamics Simulation of Nanostructured Materials: An Understanding of Mechanical Behavior*, CRC Press, Boca Raton, FL **2020**.
- [38] A. Marin-Gonzalez, J. G. Vilhena, R. Perez, F. Moreno-Herrero, *Quarterly Reviews of Biophysics* **2021**, *54*, e8.
- [39] G. Prampolini, L. Greff da Silveira, J. G. Vilhena, P. R. Livotto, *J. Phys. Chem. Lett.* **2022**, *13*, 243.
- [40] C.-A. Palma, M. Cecchini, P. Samori, *Chem. Soc. Rev.* **2012**, *41*, 3713.
- [41] S. Liese, M. Gensler, S. Krysiak, R. Schwarzl, A. Achazi, B. Paulus, T. Hugel, J. P. Rabe, R. R. Netz, *ACS Nano* **2017**, *11*, 702.
- [42] The tension of metallic films deposited by electrolysis, *Proceedings of the Royal Society of London A: Mathematical, Physical and Engineering Sciences* **1909**, *82*, 172.
- [43] X. Feng, Y.-S. Huang, A. J. Rosakis **2007**, *74*, 1276.
- [44] N. J. Tao, S. M. Lindsay, A. Rupprecht, *Biopolymers* **1989**, *28*, 1019.
- [45] N. Lavallo, S. A. Lee, A. Rupprecht, *Biopolymers* **1990**, *30*, 877.
- [46] C. Zhang, in *Encyclopedia of Tribology*, (Eds: Q. J. Wang, Y.-W. Chung), Springer US, Boston, MA **2013**, pp. 1704–1708.
- [47] B. R. Shrestha, X. Banquy, *Biointerphases* **2016**, *11*, 018907.
- [48] E. Westhof, *Annual Review of Biophysics and Biophysical Chemistry* **1988**, *17*, 125.
- [49] E. Westhof, in *Water and Biological Macromolecules*, (Ed. E. Westhof), Macmillan Education UK, London **1993**, pp. 226–243.
- [50] A. Pérez, I. Marchán, D. Svozil, J. Sponer, T. E. Cheatham, C. A. Laughton, M. Orozco, *Biophys. J.* **2007**, *92*, 3817.

- [51] W. D. Cornell, P. Cieplak, C. I. Bayly, I. R. Gould, K. M. Merz, D. M. Ferguson, D. C. Spellmeyer, T. Fox, J. W. Caldwell, P. A. Kollman, *Journal of the American Chemical Society* **1996**, *118*, 2309.
- [52] A. T. Guy, T. J. Piggot, S. Khalid, *Biophys. J.* **2012**, *103*, 1028.
- [53] M. Nakano, H. Tateishi-Karimata, S. Tanaka, F. Tama, O. Miyashita, S. ichi Nakano, N. Sugimoto, *Chem. Phys. Lett.* **2016**, *660*, 250.
- [54] A. Marin-Gonzalez, J. G. Vilhena, R. Perez, F. Moreno-Herrero, *Proceedings of the National Academy of Sciences* **2017**, *114*, 7049.
- [55] J. G. Vilhena, E. Gnecco, R. Pawlak, F. Moreno-Herrero, E. Meyer, R. Pérez, *J. Phys. Chem. B* **2018**, *122*, 840.
- [56] J. Wang, R. M. Wolf, J. W. Caldwell, P. A. Kollman, D. A. Case, *J. Comput. Chem.* **2004**, *25*, 1157.
- [57] J.-L. Tsai, J.-F. Tu, *Mater. Design* **2010**, *31*, 194.
- [58] J. E. Andrews, S. Sinha, P. W. Chung, S. Das, *Phys. Chem. Chem. Phys.* **2016**, *18*, 23482.
- [59] J. P. Brandt, T. W. Patapoff, S. R. Aragon, *Biophys. J.* **2010**, *99*, 905.
- [60] M. Pykal, P. Jurecka, F. Karlicky, M. Otyepka, *Phys. Chem. Chem. Phys.* **2016**, *18*, 6351.
- [61] M. Kabeláč, O. Kroutil, M. Předota, F. Lankaš, M. Šíp, *Phys. Chem. Chem. Phys.* **2012**, *14*, 4217.
- [62] H. S. Kim, S. M. Huang, Y. G. Yingling, *MRS Adv.* **2016**, *1*, 1883.
- [63] S. K. Min, W. Y. Kim, Y. Cho, K. S. Kim, *Nat. Nanotechnol.* **2011**, *6*, 162.
- [64] I. S. Joung, T. E. Cheatham, *J. Phys. Chem. B* **2009**, *113*, 13279.
- [65] W. L. Jorgensen, J. Chandrasekhar, J. D. Madura, R. W. Impey, M. L. Klein, *J. Chem. Phys.* **1983**, *79*, 926.
- [66] G. Raffaini, F. Ganazzoli, *Macromol. Biosci.* **2007**, *7*, 552.
- [67] D. A. Case, T. A. Darden, T. E. C. III, C. Simmerling, J. Wang, R. Duke, R. Luo, R. Walker, W. Zhang, K. Merz, B. Roberts, S. Hayik, A. Roitberg, G. Seabra, J. Swails, A. Götz, I. Kolossváry, K. Wong, F. Paesani, J. Vanicek, R. Wolf, J. Liu, X. Wu, S. Brozell, T. Steinbrecher, H. Gohlke, Q. Cai, X. Ye, J. Wang, M.-J. Hsieh, et al., *AMBER12*, University of California, San Francisco **2012**.
- [68] A. W. Götz, M. J. Williamson, D. Xu, D. Poole, S. Le Grand, R. C. Walker, *J. Chem. Theory Comput.* **2012**, *8*, 1542.
- [69] R. Salomon-Ferrer, A. W. Götz, D. Poole, S. Le Grand, R. C. Walker, *J. Chem. Theory Comput.* **2013**, *9*, 3878.
- [70] M. Crowley, T. Darden, T. Cheatham, D. Deerfield, *The Journal of Supercomputing* **1997**, *11*, 255.
- [71] U. Essmann, L. Perera, M. L. Berkowitz, T. Darden, H. Lee, L. G. Pedersen, *J. Chem. Phys.* **1995**, *103*, 8577.
- [72] R. J. Loncharich, B. R. Brooks, R. W. Pastor, *Biopolymers* **1992**, *32*, 523.
- [73] D. R. Roe, T. E. Cheatham, *J. Chem. Theory Comput.* **2013**, *9*, 3084.
- [74] M. L. Connolly, *J. Appl. Crystallogr.* **1983**, *16*, 548.